Monthly Notices of the ROYAL ASTRONOMICAL SOCIETY

MNRAS **519,** 5567–5578 (2023) https://doi.org/10.1093/mnras/stad054
Advance Access publication 2023 January 13

Bending the rules of PAH hydrogenation: the case of corannulene

Mirko Leccese [1]★ R. Jaganathan,[2]★ L. Slumstrup,[2] J. D. Thrower [2] L. Hornekær[2,3] and R. Martinazzo[1]

[1]*Department of Chemistry, Università degli Studi di Milano, Via Golgi 19, Milan, I-20133, Italy*
[2]*Center for Interstellar Catalysis (InterCat), Department of Physics and Astronomy, Aarhus University, Ny Munkegade 120, Aarhus C, DK-8000, Denmark*
[3]*Interdisciplinary Nano-Science Centre (iNano), Aarhus University, Gustav Wieds Vej 14, Aarhus C, DK-8000, Denmark*

Accepted 2023 January 5. Received 2022 December 31; in original form 2022 October 30

ABSTRACT

The interaction of a curved polycyclic aromatic hydrocarbon (PAH), corannulene ($C_{20}H_{10}$), with H-atoms leading to the formation of highly superhydrogenated species was studied. In particular, we determined the H-atom addition sequence to a monolayer of corannulene deposited on a graphite surface in order to understand the effect of curvature on the interaction of PAHs with H-atoms. We also investigated why superhydrogenated corannulene species with a certain number of additional H-atoms are more stable than the others. A combination of thermal desorption mass spectrometry measurements and density functional theory calculations was used to reveal and understand the presence of the most stable configurations in the superhydrogenation sequence of corannulene. Specifically, the experiments demonstrate the presence of stable configurations of superhydrogenated corannulene at specific hydrogenation levels of 2, 6, 8, 10, 12, 14, 16, 17, and 18 extra H-atoms. Density functional theory calculations of binding energies and barrier heights explain why some of these configurations are particularly stable and provide new insights into the superhydrogenation of curved PAH molecules under interstellar conditions.

Key words: astrochemistry – molecular processes – methods: laboratory: molecular – ISM: molecules.

1 INTRODUCTION

There is a general consensus that polycyclic aromatic hydrocarbons (PAHs) are the carriers of infrared emissions with main features at 3.3, 6.2, 7.7, 8.6, 11.3, and 12.7 μm detected from various interstellar objects (Leger 1984; Peeters et al. 2004; Salama 2008; Tielens 2008) termed as the aromatic infrared bands (AIBs). In addition, PAHs are also suggested to be possible carriers of the diffuse interstellar bands (DIBs; Léger & d'Hendecourt 1985; Duley 2006) that are absorption features seen in the spectra of astronomical objects in the Milky Way and other galaxies. Several infrared (IR) bands and DIBs have also been attributed to C_{60}, C_{70}, and C_{60}^{+} (Cami et al. 2010a; Campbell et al. 2015).

In regions of the interstellar medium (ISM) with low UV flux, PAHs are expected to be mainly neutral and possibly superhydrogenated (hereafter referred to as HPAHs; Bakes & Tielens 1998a). The interaction of PAHs and HPAHs with H-atoms is of interest in terms of H_2 formation, as well as with respect to the stability of PAHs and HPAHs under interstellar conditions (Bauschlicher 1998; Rauls & Hornekær 2008; Cazaux et al. 2016; Cassam-Chenaï, Pauzat & Ellinger 1994; Bakes & Tielens 1998b; Le Page, Snow & Bierbaum 2003; Rapacioli et al. 2018; Wolf et al. 2016; Reitsma et al. 2014; Gatchell et al. 2015; Thrower et al. 2012). Theoretical investigations of PAH hydrogenation have shown that H_2 formation through abstraction reactions is feasible from HPAHs (Rauls & Hornekær 2008; Cazaux et al. 2016; Ferullo, Zubieta & Belelli 2019). These results have been confirmed by experiments (Thrower et al. 2012, 2014; Skov, Thrower & Hornekaer 2014; Cazaux et al. 2019; Mennella et al. 2011, 2021). Studies have also demonstrated that the edge structure of the PAH or HPAH determines its stability and its chemical reactivity (Jochims, Baumgärtel & Leach 1999; Campisi et al. 2020; Stockett et al. 2021; Tang et al. 2022; Jaganathan et al. 2022).

PAHs can display an intrinsic curvature that can be due either to their structure or, simply, their size. For example, if one replaces the inner 6-membered ring of coronene with a 5-membered ring, the resulting structure, called corannulene ($C_{20}H_{10}$), is bowl-shaped (Nestoros & Stuparu 2018). On the other hand, accurate theoretical investigations have shown that coronenes ($C_{6N^2}H_{6N}$) attain an umbrella-like equilibrium geometry as soon as $N \gtrsim 9-12$ (depending on the theory level), thereby suggesting that planarity is lost also in regular PAHs, if sufficiently large (Karadov 2016). Such structural deformation signals that curvature plays a key role in large PAHs and, by extension, in graphene. At the same time, it contrasts with chemical intuition that ascribes additional stability to these systems as a result of the extended π-conjugation they host. Curvature in PAHs can also be induced by partial hydrogenation: taking again coronene as an example, when a few atomic positions are hydrogenated, partly disturbing the aromaticity, the molecule undergoes a structural distortion which often appears as a surface bending (Thrower et al. 2012).

Like their planar relatives, curved PAHs are under scrutiny for the role they might play in the ISM. For instance, it has been suggested that the inclusion of non-planar components in aromatic structures induces spectral patterns similar to the AIBs (Galuè & Leines 2017; Sundararajan et al. 2018). In addition, superhydrogenated

★ E-mail: mirko.leccese@unimi.it (ML); rijutha@phys.au.dk (RJ)

forms of curved PAHs may act as sources of small molecules such as H_2 in photodissociation regions as IRMPD spectroscopy of the corannulene radical cation has demonstrated that H, H_2, and C_2H_y losses are the three main fragmentation channels (Galué et al. 2011). While PAHs are believed to account for 5–10 per cent of the interstellar carbon (Tielens 2013), fullerenes have been detected in minute amounts, $\approx 10^{-4}$ of the interstellar carbon in various environments (Omont & Bettinger 2021). C_{60} was first identified in young planetary nebulae in 2010 (Cami et al. 2010b), and it is the only fullerene that is widely detected from its weak mid-IR features (Omont & Bettinger 2021; Cami et al. 2018). At present, how fullerenes (in particular C_{60}) can form in the ISM is still debated (Candian, Zhen & Tielens 2018). They could form, either from the surface decomposition of SiC grains in hydrogen-dominated gas (Bernal et al. 2019) or via UV processing of larger PAHs. In the latter case, corannulene-like structures likely represent an intermediate step (Berné & Tielens 2012). Corannulene can thus be considered as a precursor in the synthesis of fullerenes (Kroto 1988; Pope, Marr & Howard 1993; Crowley et al. 1995). Energetic processing of hexagonal-based PAHs can also lead to carbon atom loss and formation of pentagons in the molecule (Berné & Tielens 2012; West et al. 2014; Bouwman, de Haas & Oomens 2016; Petrignani et al. 2016; De Haas, Oomens & Bouwman 2017; Omont & Bettinger 2021). Therefore, it is very likely that PAHs with 5-membered rings will be present in certain regions of the ISM such as photodissociation regions (PDRs; Bernal et al. 2019).

In these respects, corannulene is one of the most interesting members of the family of curved PAHs. Both terrestrial experiments (Lovas et al. 2005) and astronomical observations of the DIBs suggest its presence in the ISM (Bernstein et al. 2018). The electron density of corannulene differs between its concave and convex faces, thereby giving rise to a sizeable molecular dipole moment of 2.07 ± 0.02 debye (Thaddeus 2006). This property makes the PAH promising for detection in the radio and microwave region of the electromagnetic spectrum. Observational studies have so far been unsuccessful in identifying corannulene in the ISM (Thaddeus 2006; Pilleri et al. 2009), though corannulene has been observed in the Allende Meteorite (Becker & Bunch 1997). The formation mechanism of the corannulene molecule in the ISM medium is still under debate. However, recent terrestrial experiments mimicking carbon-rich circumstellar environments have shown that formation of bucky-bowl structures could occur in ring-expansion reactions involving planar radical PAHs (Zhao et al. 2019, 2021). The interaction of corannulene with H-atoms has been studied, mainly in the context of H-storage and organic electronics due to its unique properties e.g. bowl-to-bowl inversion at room temperature (Scanlon et al. 2006; Nestoros & Stuparu 2018). By means of muon-spin-resonance techniques at 40 K and 410 K and H_2-sorption experiments at 77 K, Gaboardi et al. (2019) found that corannulene has a high affinity towards the formation of hydrogenated species. The authors of this study further argued that partial hydrogenation would be more likely as the fully superhydrogenated corannulene ($C_{20}H_{30}$) would be highly distorted and unstable.

Corannulene is the simplest molecule on which one can study the influence of curvature on the structural and chemical properties, with the possibility of a direct comparison with the planar, well-studied analogue coronene. These characteristics of corannulene and its potential role in ISM chemistry have thus motivated this combined experimental and theoretical study of the interaction of neutral corannulene with H-atoms and the identification of the H-atom addition sequence and stable superhydrogenated species. Our findings are then compared with those of a similar study performed on the closest planar relative, coronene, by Jensen et al. (2019), and the influence of curvature on PAH reactivity is elucidated.

2 METHODS

2.1 Experimental methods

Temperature-programmed desorption experiments were performed under ultra-high vacuum conditions (UHV), with typical base pressures of 10^{-10} mbar. The corannulene ($C_{20}H_{10}$) monolayer was grown on a clean highly oriented pyrolitic graphite (HOPG) substrate by thermal evaporation of bulk corannulene (TCI, >97.0 per cent) from a home-built Knudsen cell-type source, operated at a temperature of 353 K. During corannulene deposition, the sample temperature was held below 210 K as corannulene has a significant desorption rate even at room temperature.

The corannulene monolayer films were then exposed to a beam of H-atoms produced using a commercial hot capillary thermal cracker. The sample temperature was kept below 210 K. The hydrogen atom beam source (HABS) (Tschersich, Fleischhauer & Schuler 2008) was operated at a temperature of 2300 K at which it efficiently dissociates H_2. The HABS was fitted with a curved quartz nozzle to cool the H-atoms to approximately 1000 K through multiple collisions with the nozzle walls. The shape of the nozzle ensures at least four collisions between the hot H-atoms and the inner surface of the nozzle. Ioppolo et al. (2013), used a similar nozzle design and argued that it resulted in cooling of the H-atoms to 300 K. Inelastic scattering simulations with the hard-cube model (Grimmelmann, Tully & Cardillo 1980), estimated the H-atom beam temperature to be ≈1500 K (Simonsen 2020). This estimate should be viewed as a upper bound to the beam temperature, since modelling does not account for further cooling effects, e.g. trapping-desorption or collisions with lighter surface elements other than those assumed in the simulation (Fan & Manson 2009). Hence, we assume, 300 K $\leq T_{\text{H-atoms}} <$ 1500 K. The H-atom flux was estimated to be $(6 \pm 3) \times 10^{14}$ atoms $\text{cm}^{-2}\text{s}^{-1}$ through calibration measurements of H-atom uptake and exchange with D-atoms on a reconstructed Si(100)–(2×1) surface (Simonsen 2020).

The temperature-programmed desorption measurements were performed by increasing the sample temperature by 1 Ks^{-1}, while collecting the desorption products with a quadrupole mass spectrometer (QMS; Extrel CMS LLC) capable of detecting species with mass-to-charge ratios (m/z) of up to 500. Pristine corannulene has a mass of 250 amu and so singly ionized corannulene has $m/z = 250$, while singly ionized fully hydrogenated corannulene with 20 additional hydrogen atoms has $m/z = 270$. The QMS was set up to scan the range $m/z = 50-320$, where the lower limit ensured detection of possible fragmentation products and the upper limit was chosen to establish a signal baseline, as no species with such masses should be present. Here, data are presented in the range $m/z = = 240$–280 as the focus is on H-addition to corannulene. The thermal desorption traces were integrated to obtain the absolute yield of each of the desorbed species from which the mass distributions presented here were obtained.

2.2 Computational methods

The density functional theory (DFT) calculations were performed with the M06-2X meta-hybrid GGA exchange-correlation function (Zhao & Thrular 2008), which turned out to be the best-performing functional for investigating HPAHs (Jensen et al. 2019; Campisi et al. 2020). We employed spin-unrestricted wavefunctions in conjunction with a 6-311G(d,p) atom-centred basis set, using tight convergence

criteria on both the electronic and structural optimizations, as defined in Gaussian16 (Frisch et al. 2016). Optimized structures were checked with harmonic frequency calculations. Binding energies for the addition of H-atoms, D, were computed for a number of sites, i, according to the following expression:

$$D_i^{n+1} = E_\star^n + E_{\rm H} - E_i^{n+1},$$

where $E_\star^n$ is the DFT energy of the most stable isomer with n additional hydrogen atoms, $E_{\rm H}$ is the energy of a H-atom, and E_i^{n+1} is the energy of the structure with an additional H-atom at site i. Henceforth the symbol, $\star$, will be used to denote the most stable site, i.e. $D_\star^n \equiv \max_i\{D_i^n\}$. The plausible adsorption sites (typically 3–4 per step) were selected with the help of 'chemical intuition', as described in detail in our previous studies on coronene (Jensen et al. 2019) and pentacene (Campisi et al. 2020), and the hydrogenation sequence was continued by selecting, at each step, the structure with the largest binding energy. Energy barriers were computed for the most relevant cases only, by performing a transition-state search to locate the saddle point on the system potential energy surface. Frequency analysis was always performed to confirm the nature of the stationary point found.

3 RESULTS AND DISCUSSION

3.1 Experiments

The product mass distributions obtained after exposing a monolayer of corannulene to an increasing fluence of H-atoms are presented in Fig. 1. The product yields in the range m/z = 251–271, plotted in yellow, have been corrected for the ^{13}C contribution. This was done by subtracting the fraction of ^{13}C, calculated by combining the natural abundance of ^{13}C and the number of carbon atoms in corannulene, from each yield in the range m/z = 251–271. Panel (a) of Fig. 1 shows the mass distribution of the desorption products for the pristine corannulene monolayer in which the prominent peak is seen at m/z = 250 (corannulene), as expected. The smaller peaks just below m/z = 250 can be accounted for by nH loss during the ionization step in the QMS.

Panels (b)–(f) in Fig. 1 show that when the pristine corannulene monolayer is exposed to H-atoms, the yield of m/z = 250 becomes lower, and peaks at both higher and lower masses appear. The peaks at masses below m/z = 250 correspond to fragments, while those between m/z = 251 and 270 correspond to superhydrogenated corannulene species. In particular, the peaks at lower masses (m/z = 221–224) can be attributed to the loss of C_2H_y either on the surface (as a consequence of the hydrogenation reaction) or in the QMS. In panel (c) of Fig. 1, a clear odd–even alternation is seen for the superhydrogenated species. The species with an even number of added H-atoms (n = 2, 6, 8, 10, 12, and 14) have higher yields than their neighbouring odd-mass species. This indicates the stability of the even-mass species towards further H-addition due to the lower reactivity of closed-shell species. However, in panel (d) of Fig. 1, the odd–even alternation is disrupted by the species with n = 17, m/z = 267, which has a higher yield than its neighbouring even-mass species. In panels (d), (e), and (f) of Fig. 1, a small yield of the fully superhydrogenated product n = 20 ($C_{20}H_{30}$), m/z = 270, is observed. Even at exposure to a H-atom fluence of 8.6 × 10^{18} atoms cm^{-2}, the fully superhydrogenated corannulene species (m/z = 270) does not have a high yield and the products with n = 16, 17 and 18 dominate the distribution. It is observed that exposure of the monolayer to fluences greater than 8.6 × 10^{18} atoms cm^{-2} does not change the mass distribution further and hence panel (f) represents a saturated steady state.

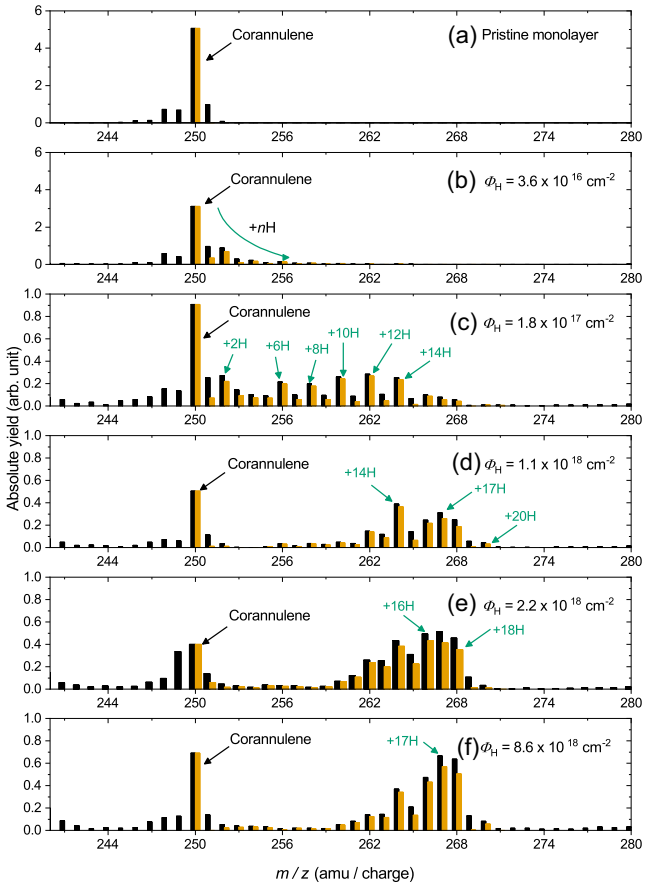

Figure 1. Desorption product mass distributions obtained following exposure of a monolayer of corannulene to H-atom fluences (Φ_H) ranging from 0 to 8.6 × 10^{18} atoms cm^{-2} as indicated on each panel. The product yields in the range m/z = 251–271 have been corrected for ^{13}C contribution and plotted in yellow while the measured yield is plotted in black. In panel (c), the prominent superhydrogenated species are marked with the number of H-atoms added to the corannulene molecule (n) that they correspond to. A clear odd–even alternation is seen. In panels (d), (e), and (f), the species with n = 17 is observed to be a dominant species along with n = 16 and n = 18. Only a small yield of the fully superhydrogenated species (n = 20) with m/z = 270 is observed.

3.2 Calculations

As indicated by earlier studies on coronene and pentacene (Thrower et al. 2012; Jensen et al. 2019; Campisi et al. 2020), the appearance of prominent peaks at specific m/z indicates that certain superhydrogenated configurations are more stable than others and that sizeable barriers exist for further H-addition to these stable configurations. To identify such stable hydrogenated structures, an extensive DFT investigation of the step-wise hydrogenation sequence of corannulene was carried out and is presented here.

Before discussing the lowest energy H-atom addition pathway, we begin by comparing corannulene with coronene in order to highlight the main differences and similarities between these closely related molecules. Both of them are characterized by three non-equivalent sites that differ in the π-coordination number (Z): two- and three-coordinated sites on the edges, and three-coordinated sites in the inner ring, which we refer to, respectively, as outer-edge, inner-edge

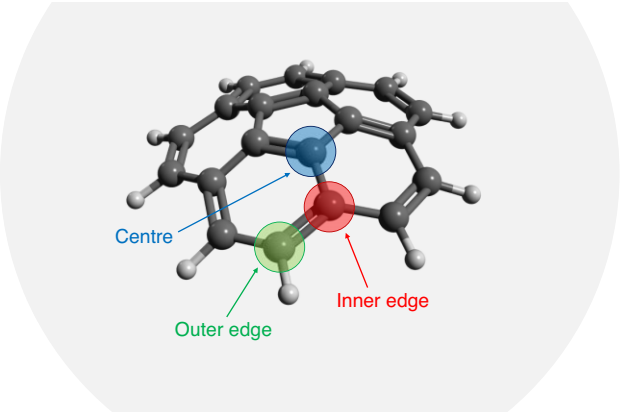

Figure 2. Molecular structure of corannulene ($C_{20}H_{10}$; $m/z = 250$) with the three non-equivalent sites – outer-edge, inner-edge and centre site marked in green, red, and blue, respectively.

Table 1. Binding energies, D (eV), and adsorption barriers, E_b (meV), for the first hydrogenation of the three non-equivalent sites of corannulene ($C_{20}H_{10}$) and coronene ($C_{24}H_{12}$). All values are zero-point energy corrected. Also reported for corannulene the pyramidalization angles θ_P and the percentage of the s fraction of the π-like orbital (w_π %), both of which vanish for the planar coronene molecule. See Appendix B for the details of the calculation.

	Corannulene				Coronene	
Site	D	E_b	θ_P	w_π per cent	D	E_b
Outer-edge	1.37	180	1.6°	0.2 %	1.11	235
Inner-edge	0.76	296	3.8°	0.9 %	0.37	446
Centre	1.23	155	8.4°	4.1 %	0.30	423

and centre sites For corannulene, these are shown in Fig. 2. Formally, replacing the six-membered ring of coronene with a five-membered one to make corannulene has two major consequences. Firstly, from the topological point of view, it makes corannulene a non-alternant hydrocarbon. By contrast, coronene is alternant (or 'bipartite') – its carbon atoms form two disjoint sets with no bond occurring between atoms of the same set – and as such it displays an interesting symmetry in the electronic spectrum (the '*e*-*h* symmetry') that affects its chemical reactivity. Secondly, the presence of a five-membered ring bends the structure and confers it its characteristic bowl shape. To estimate its curvature, the corannulene lattice can be conveniently assimilated to a polyhedral surface, with vertexes located at the carbon atom positions. On polyhedral surfaces, curvature builds up at any vertex V that displays a non-vanishing angular defect, $K = 2\pi - \sum_i \beta_i$, where the sum runs over the faces i sharing V and β_i are the angles of their corners at V. For the optimized structure of corannulene $K \approx 6.4°$ at the carbon atoms in the five-membered ring, which is about half the value of the angular defect per site in C_{60} [namely $360° - (2 \times 120° + 108°) = 12°$ or, equivalently, $2 \times 360°/60 = 12°$].

From a chemical point of view, curvature involves a pyramidalization of the carbon atoms and a re-hybridization of their valence orbitals. Table 1 reports the pyramidalization angle (θ_P) at the different corannulene sites, as given by the orientation of the pyramid axis there.[1] A substantial pyramidalization of the carbon atoms in the inner ring is observed, with $\theta_P \approx 8.4°$. On the other hand, the outer-edge and inner-edge sites are less affected by re-hybridization, with θ_P not exceeding 4°. From a purely geometrical perspective, the centre sites of corannulene are found in a configuration that most closely resembles sp^3 (for which $\theta_P = 19.5°$), which is the ideal final configuration after H-addition. This translates into larger binding energies and reduced barriers to addition.

Table 1 also summarizes the energetics of H-atom addition to the three non-equivalent sites in both corannulene and coronene. Owing to the strong re-hybridization, the centre and the outer-edge sites of corannulene display a comparable hydrogen affinity in contrast to what is seen for coronene. In coronene, planarity, and bipartitism contribute to marked edge localization of the frontier orbitals that gives rise to remarkably large binding energies and small adsorption barriers on the outer-edge sites. In corannulene, the intrinsic curvature attenuates such an edge localization and increases the reactivity of centre sites. At the outer edges the undercoordination ($Z = 2$) remains effective in making the sites reactive, but it no longer represents a net driving force for the hydrogenation reaction. Also, it is noteworthy that, for corannulene, the barrier to stick hydrogen to the centre sites is smaller (by ≈2.5 meV) than on the outer-edge sites, as the surface is to some extent already puckered around these positions.

From the very first H-addition step, we have considered two different hydrogenation pathways that leads to the fully superhydrogenated molecule. The first path starts with the hydrogenation of the most stable site (the outer edge one), thereby assuming that H-atoms are energetic enough to overcome the large adsorption barrier there. A second path, on the other hand, starts with the lowest barrier site (the centre site), hence it is assumed that the adsorption process is under kinetic control. In both cases, the hydrogenation sequence is continued by selecting, at each hydrogenation step, the structure with the largest binding energy ($D^n_\star$). A path started from the inner edge was excluded from the investigation, because the large barrier to stick the H on such site suggests that it would be kinetically inhibited, at least compared to the other two pathways mentioned above.

The first addition pathway is shown in panel (a) of Fig. 3 with the number on the carbon atoms showing the sequence of H-atom addition. The energetics along this path are displayed in panel (b) of Fig. 3, which reports the sequential H-atom adsorption energy (D^n_i) as vertical bars. In the same figure, red triangles are used to represent the height of the adsorption barriers that separate the most stable nth hydrogenated structure from the $(n + 1)$th one, if not vanishing, and green rectangles highlight barrierless steps.

As observed for coronene (Jensen et al. 2019), the energetics of H-addition shows an evident even–odd alternation arising from the larger exothermicity of radical-radical reactions that result in even-numbered species ($C_{20}H_{10+2n}$). The amplitude of this oscillation (≈1.8 eV) can be considered as a rough measure of the π-bond strength, since breaking of a π bond is required only when forming an odd-numbered species, provided of course the molecule is in its ground-state, which is a singlet (doublet) for n even (odd). This 'oscillation amplitude' is smaller than that found for coronene (≈2.5 eV), indicating a reduction of the π-bond strength, as a consequence of the smaller overlap between π-orbitals.

The largest binding energies are found for corannulene with a specific number of added H-atoms, namely $D^n_\star = 3.63$, 3.33, 3.38, 3.28, 3.47, 3.75, 3.29, and 3.37 eV for $n = 4$, 6, 8, 10, 12, 14, 16, and

[1]The pyramid axis is the unique axis which forms *equal* angles with three non-collinear vectors originating from a common point, here the bonds linking a C atom with its neighbours. The pyramidalization angle is then this common (obtuse) angle *minus* $\pi/2$.

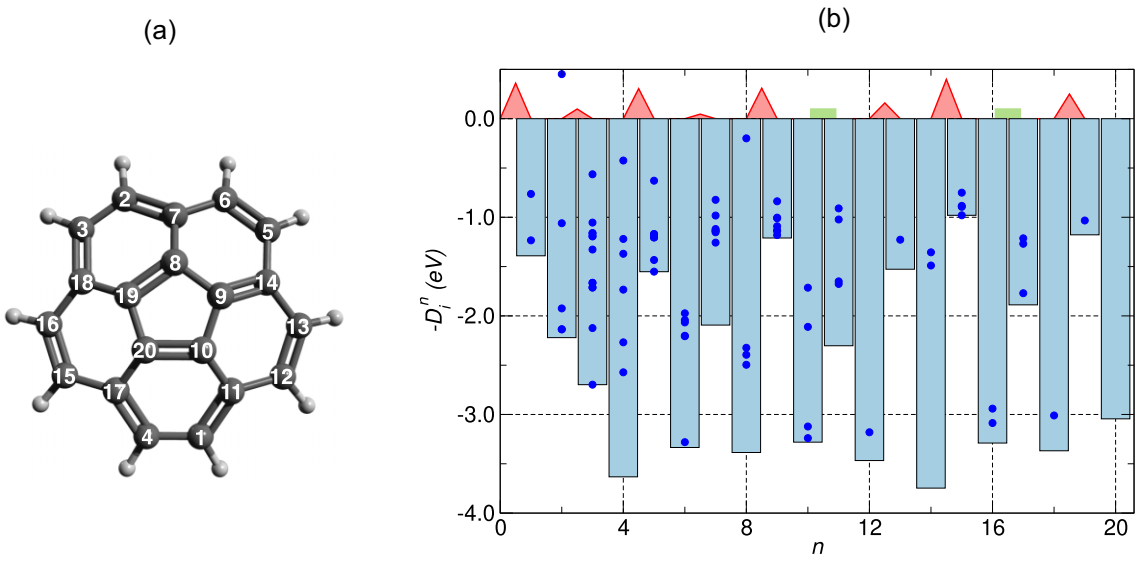

Figure 3. (a) 'Thermodynamic' hydrogenation sequence of the corannulene molecule, starting with H-addition to the most stable outer-edge site. The numbers $i = 1, 2,...,n$ indicate, schematically, the lowest energy isomer with n extra H-atoms, $C_{20}H_{10+n}$. (b) Hydrogen adsorption energy (light blue bars) along the main sequence shown in (a). The energies for alternative, less stable (or unstable) hydrogenation configurations with the same number of extra H-atoms are shown as dots. A red triangle between n and $n+1$ represents the height of the barrier for sticking a H-atom to the n-times hydrogenated corannulene (meV, multiplied by a factor of 2 to make it visible on the scale of the graph). Green rectangles denote barrierless steps. All values are zero-point energy corrected.

Table 2. Energy barriers (meV) for forming the corannulene superhydrogenated species with n added H-atoms ($C_{20}H_{10+n}$) along the first pathway depicted in Fig. 3(a).

n	Energy barrier
1	180
3	49
5	152
7	23
9	155
11	0.0
13	80
15	199
17	0.0
19	125

18, respectively. The stability of these species is further corroborated by the appearance of sizeable barriers to further sticking, E_b (reported in Table 2), which are known to correlate well with D (i.e. the larger the binding energy, the smaller the addition barrier into that state; Evans & Polanyi 1938).

The largest adsorption barriers for the reaction $C_{20}H_{10+n} + H \rightarrow C_{20}H_{10+(n+1)}$ are found for $n = 4$, 8, 12, 14, and 18, thus indicating a greater stability of these hydrogenated species. Overall, these results are in good agreement with the experimentally obtained mass distributions shown in Fig. 1 with a few exceptions that are discussed in the following paragraphs.

First, $n = 4$ is not found to accumulate in the experiments, even though, according to the DFT calculations and theoretical considerations, it should be rather stable towards further hydrogenation since the latter would require considerable loss of resonance stabilization. This is evidenced by the Clar's formulae (Clar 1972) – chemical formulae with the maximum number of π sextets – and their 'degeneracy', which give a rough measure of the aromatic stabilization. In pristine corannulene, the maximum number of Clar's sextets, also known as Clar's number C, is two and there exist *five* possible Clar's formulae presenting two sextets (see Fig. A1). As H-atoms are attached to the molecule, the number of Clar's formulae with two π-sextets progressively reduces, and the 'Clar's degeneracy' is fully removed when hydrogenating the $n = 4$ structure, regardless of the reaction site. Therefore, at least in the gas phase, $n = 4$ is expected to be an 'obstacle' towards full hydrogenation of a corannulene molecule, as witnessed by the large DFT barrier (≈152 meV) found for this structure. Hence, the absence of the accumulation of the superhydrogenated corannulene with $n = 4$ in the experiments may be due to an interaction with the substrate, which could facilitate the addition of the next H-atom.

For $n = 6$ and $n = 10$, the situation is somewhat reversed. These structures are found to accumulate in the experiments even though the computed barriers for their hydrogenation are small or even vanishing.

The $n = 14$ species dominates the experimentally determined mass distribution at exposure to intermediate fluences. Its great stability is confirmed by our calculations, according to which $n = 14$ has the largest binding energy (≈ 3.74 eV) and also the largest barrier to further sticking (≈200 meV). As it was observed for coronene, the stability of this species can be traced back to the presence of the aromatic ring left in the molecule (see Fig. A1 for the Clar structure). Its hydrogenation determines the complete loss of aromaticity and requires extra energy compared to the previous steps.

The accumulation of the species $n = 16$, 17, and 18, together with the absence of an intense peak for the fully hydrogenated molecule ($n = 20$), is a remarkable feature of the experimentally obtained mass distribution of corannulene that strongly contrasts to what was observed for coronene (Jensen et al. 2019). While the large binding energy and a large barrier to further sticking confirm the stability of $n = 18$, the lower stability of $n = 20$ with respect to $n = 18$ and the large barrier to add the 19th H-atom may partly prevent the formation of fully hydrogenated corannulene, thereby accounting for its low yield in the experiments. The energetics of Fig. 3(b) cannot account for the experimentally observed prominent peaks at $n = 16$ and 17.

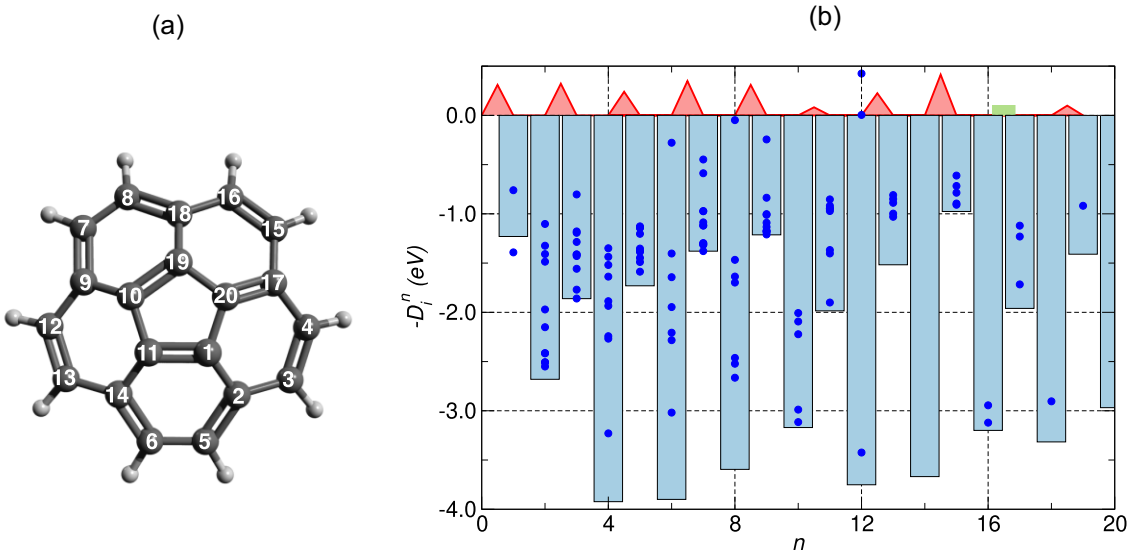

Figure 4. Energetics along the second hydrogenation pathway considered, originating from the first H addition on the centre site. Vertical bars indicates (minus) the binding energy of the *n*th hydrogen; red triangles indicates the barrier of the n to $n + 1$ (meV, multiplied by 2); green rectangles denotes barrier-less steps; and blue dots marks the binding energies of additional sites considered at each hydrogenation step. All values are zero-point energy corrected.

Panel (b) of Fig. 3 also shows the binding energies of less stable hydrogenated configurations (blue dots). Some of these values are close to $D_\star^n$, thereby suggesting the possibility of branching points also in the hydrogenation sequence of corannulene.

As mentioned above, in considering a second alternative pathway, we decided to start by hydrogenating the centre site which has the smallest barrier height for the first hydrogenation step. The resulting sequence is shown in panel (a) of Fig. 4, while the corresponding energetics along this path is displayed in panel (b). Overall, the results parallel those found along the first pathway, but some noteworthy differences appear. In particular, this second pathway displays a better agreement with the experiment at low n's ($n = 1-10$). Indeed, a sizeable barrier is detected for the hydrogenation of $n = 6$ (Table 3), indicating great stability of this structure which is found to accumulate in the experimentally obtained mass distribution. By the same token, in contrast to the first path, a barrier is found to hydrogenate $n = 10$, though small (41 meV). On the other hand, a worse agreement with the experiment is found at high n's ($n = 15-20$). For instance, a smaller barrier (49 versus 125 meV) is found to hydrogenate $n = 18$, at odds with the mass distribution that show the accumulation of this structure. Noteworthy, $n = 4$ is again a very stable structure although a smaller barrier for hydrogenation is found for this hydrogenation sequence.

We notice that the two hydrogenation sequences look identical from $n = 14$ onwards. However, the pathways cannot cross because of a different buckling of the molecule already from $n = 2$, which leads to different energies for high n's along the two sequences. The optimized structures of n-hydrogenated corannulene (for $n = 1$–20) along both sequences described above are shown in Appendix C.

Considering either sequences, the findings for corannulene with $n = 17$ extra hydrogens are undoubtedly the most unexpected, since odd-numbered species are found to be unstable towards further hydrogenation and should not accumulate in the mass distributions. To understand why $n = 17$ accumulates in the experimental results, we investigated alternative mechanisms to H-addition that may be operative under experimental conditions and can contribute to its formation.

Table 3. Energy barriers (meV) for forming the n-times corannulene super-hydrogenated species ($C_{20}H_{10+n}$) along the second sequence investigated, depicted in Fig. 4.

n	Energy barrier
1	155
3	161
5	120
7	175
9	155
11	41
13	112
15	207
17	0.0
19	49

Table 4. Energies (ΔE, eV) and barriers (E_{ab}, meV) for the H abstraction reaction $C_{20}H_{10+n} + H \rightarrow C_{20}H_{10+(n-1)} + H_2$, along with adsorption energies $-D_\star^n$ (eV) and energy barriers (E_b, meV) for H addition, $C_{20}H_{10+n} + H \rightarrow C_{20}H_{10+(n+1)}$.

n	Abstraction		Addition	
	ΔE	E_{ab}	$-D_\star^n$	E_b
16	−1.08	161	−1.89	0.0
17	−2.48	0.0	−3.37	0.0
18	−1.00	120	−1.18	125
19	−3.20	0.0	−3.04	0.0

First, we considered the direct abstraction of a H-atom by a gas-phase H projectile, $C_{20}H_{10+n} + H \rightarrow C_{20}H_{10+(n-1)} + H_2$, according to what is known as the Eley–Rideal mechanism. Table 4 reports the

Table 5. Desorption energies (ΔE, eV) for different dimer configurations: *i–c* (inner edge–centre), *o–o* (outer edge–outer edge), *i–o* (inner edge–outer edge), *c–c* (centre–centre), and *para*.

Configuration	ΔE
i–c	0.17
o–o	4.01
i–o	1.00
c–c	0.93
Para	0.29

abstraction energies

$$\Delta E = E(H_2) + E(C_{20}H_{10+(n-1)}) - (E(H) + E(C_{20}H_{10+n}))$$

and the corresponding barriers for the relevant steps, along with the adsorption energies and barriers for the H addition reaction, $C_{20}H_{10+n} + H \rightarrow C_{20}H_{10+(n+1)}$. Apart from the case for $n = 16$, the emerging picture is that H-abstraction and H-addition compete with each other since the abstraction barrier either matches the sticking barrier or differs by a few meV only, as on graphitic surfaces (Casolo et al. 2009). The sizable barrier for the abstraction out of $n = 16$, in conjunction with the larger exothermicity found for the abstraction process (compared to H-attachment) in $n = 19$, may partially explain the accumulation of the species in the range $n = 16$–18. In addition, we note that, in contrast to coronene – that undergoes barrierless adsorption at high hydrogenation degrees – corannulene presents a barrier to add a H-atom to $n = 18$ that may further contribute to the accumulation of the species in the range $n = 16$–18.

Next, we considered the formation of $n = 17$ via desorption of H_2 from $n = 19$. When removing two H-atoms, one should consider different dimer configurations, since there is no guarantee that the backward pathway, going from the $n = 20$ to the pristine corannulene follows the same steps as H-addition to pristine corannulene. The first H-atom can be removed from 19 different positions, while the second one from 18, leading to $19 \times 18 = 324$ possible configurations, a number that cannot be reduced by symmetry arguments. The total number of H-dimers is evidently too large and out of reach to be tested; hence, we decided to focus on just a few key configurations. Following chemical intuition, we have considered four *ortho* dimers, classified on the basis of the type of binding carbon atoms (e.g. *o–o* means that the two H-atoms desorb from two ortho outer-edge sites.). In addition, for the sake of comparison, we also considered a *para* dimer and a configuration in which the two H-atoms desorb from two distant sites. The energy to desorb the dimer in a given configuration i, ΔE^i, was computed according to the equation

$$\Delta E^i = (E^i_{n=17} + E_{H_2}) - E_{n=19},$$

where $E^i_{n=17}$ is the DFT energy of the structure with $n = 17$ after the desorption of the H_2 in the dimer configuration i, $E_{n=19}$ is the energy of the structure with $n = 19$ and E_{H_2} is the energy of the H_2 molecule. The results are listed in Table 5. All reactions are found to be endothermic. The lowest reaction energy for H_2 desorption from $n = 19$ is found for the $i-c$ dimer configuration. This reaction leads to the structure $n = 17$ that forms during the onward hydrogenation pathway. In this work, we were unable to locate the transition state of the reaction and thus compute the corresponding desorption barriers. However, previous theoretical and experimental studies on graphitic surfaces indicate that both the ortho and the para H-dimer desorption require the overcoming of large barriers (≈2.5 and 1.4 eV, respectively; Hornekaer et al. 2006). On this basis and according to the computed desorption energies (Table 5), it is unlikely that $n = 17$ forms through H_2 desorption.

Other mechanisms may be considered to account for the abundance of $n = 17$, e.g. fragmentation of higher hydrogenated species or structural rearrangements. However, they are hardly captured by an unbiased DFT structural optimization, and would require further input from the experiments. In addition, the substrate used in the experiments – HOPG, may play a relevant role in this case by stabilizing the allyl radical that characterizes the $n = 17$ species.

The sequential hydrogenation of PAHs such as coronene or pentacene could be rationalized in terms of simple rules of thumb arising from the bipartitic nature of their carbon lattice. These rules, which are discussed in detail in (Jensen et al. 2019; Bonfanti et al. 2011), can be summarized as follows:

(i) When closed-shell ($S = 0$) molecules are involved, the H-atom attachment at specific lattice positions is dictated by the π-coordination and π-hyperconjugation. In particular, the H-atom preferentially sticks to undercoordinated sites ($Z = 2$ or $Z = 1$ when available) in the π-system. When more than one undercoordinated site is available, the H-atom preferentially sticks to the carbon atom with the highest π-hyper-coordination number (ξ), which is the carbon atom with the highest number of next-to-nearest neighbours in the lattice with the same coordination to hybridize with.

(ii) When open-shell molecules are involved ($S = 1/2$), the reaction is driven by the position of the unpaired electron. The latter resides in a mid-gap state that semilocalizes around the defect position (decaying as $1/r$ in the extended limit), thus making the ortho and para positions the most reactive towards the H-sticking, again with a preference for sites with small π-coordination.

As mentioned earlier, corannulene is not a bipartite lattice because of the presence of a five-membered ring and therefore the concept of π-hyperconjugation no longer applies. On the other hand, π-coordination and mid-gap-state semi-localization are still good guiding principles of the H-addition. The only step violating these rules is the second hydrogenation, where the H-atom attaches to a carbon that is distant from the first hydrogenated site, rather than preferring a closer *ortho* position. It is worth noticing that, consequently, the third hydrogenation occurs on an undercoordinated site ($Z = 1$) with a relatively large binding energy for an odd addition. The latter, in conjunction with small binding energy for the second addition, breaks the even–odd alternation initially.

One may wonder if a new rule involving pyramidalization or re-hybridization can be established to rationalize the hydrogenation sequence of corannulene. In general, there is no clear-cut correlation between the pyramidalization angle and the H-atom binding energy. The reason being that, in a molecule, both the pyramidalization and the presence of edges contribute to a different extent to increase the reactivity and their effects cannot be separated in a trivial way. Nevertheless, a close inspection of each hydrogenation level reveals that large pyramidalization angles (typically higher than 6°) in conjunction with small π-coordination determines larger hydrogen affinity. See Appendix B for details.

An additional concept that helps understanding the hydrogenation sequence of corannulene is, as mentioned above, that provided by the Clar's rule and the ensuing Clar's formulae. The rule identifies the most important Kekulè structures as those with the largest number (the Clar's number) of aromatic π-sextets (see Appendix A for details). Looking at the coroannlunene hydrogenation pathways described above, we note that up to the 8th step, both sequences develop by preserving the Clar's number of the molecule. Addition of the 9th H-atom, regardless of the position, results in the reduction

of such a number from 2 to 1. Therefore, as observed for $n = 4$, the structure with $n = 8$ extra hydrogens should represent another 'obstacle' on the road to $n = 20$, as indeed indicated by the large barrier to further sticking (155 meV). The validity of Clar's rule in determining the reactivity of the corannulene molecule underlines how the concept of aromaticity, which is originally defined for planar structures, can yet play a crucial role in curved systems as well.

4 CONCLUSIONS

The interaction of neutral corannulene with H-atoms leading to the formation of highly superhydrogenated species was studied experimentally and theoretically for the first time. The experimental results have demonstrated that a H-atom can be added to every single carbon atom in a corannulene molecule. However, even after exposure to high fluences of H-atoms, fully superhydrogenated corannulene, $C_{20}H_{30}$, was not observed to be the dominant product. This is in contrast to the findings of previous studies of coronene and pentacene hydrogenation, where the fully superhydrogenated molecules were observed to be the dominant species following exposure to a high H-atom fluence. The presence of specific stable superhydrogenated species indicate the presence of barriers to further addition. The stability of the superhydrogenated corannulene with 17 additional H-atoms, a departure from the odd–even alternation observed for other PAHs, is noteworthy.

To identify such stable hydrogenated structures, an extensive DFT investigation of the step-wise hydrogenation sequence of corannulene was carried out. Two feasible H-addition sequences were found, one with the first H-atom attaching to the outer-edge site and a second one with the first H-atom attaching to the centre site. Overall, our results compare well with the experimental data; however, some noticeable differences appear. $n = 6$, 8, 10, 12, and 14 are stable species from the experiments and the calculations also show that these species have larger binding energies than their neighbouring odd-numbered superhydrogenated species. In addition, the stability of $n = 8$ and 14 is further supported by the electronic effect of the reduction in the maximal Clar's number to 1 and 0 upon addition of the 9th and 15th H-atom, respectively. The accumulation of species in the range $n = 16$–18 and the small yield of $n = 20$ can be in part rationalized by considering the competition between H-abstraction and H-addition for $n = 17-19$ coupled with the large binding energy and presence of a barrier towards further H-addition to $n = 18$. In the experiments, the unexpected stability of $n = 17$ compared to other odd-numbered superhydrogenated species and the absence of a prominent peak at $n = 4$ are also noteworthy. This may be due to the specific experimental setting, for example, an interaction with the HOPG substrate or fragmentation patterns that exist under laboratory conditions, rather than being due to specific features of the gas-phase hydrogenated species.

In conclusion, DFT calculations in the gas-phase are able to capture most peaks of the TPD spectra, but some remain elusive and are not properly explained by competing processes such as abstraction or desorption.

Looking at the hydrogenation sequence for corannulene, we observe that π-coordination and semilocalization of the unpaired electron are still good guiding principles of the hydrogenation reaction. Interestingly, we observed that an additional concept that allows us to understand the hydrogenation sequence is that of Clar's formulae. The validity of the Clar's theory in determining the reactivity of the corannulene molecule underlines how the concept of aromaticity, which is originally defined for planar structures, can still play a crucial role also in curved systems.

The identification of superhydrogenated PAH molecules is a first essential step to understand the catalytic role of PAHs in the interstellar chemistry. This work adds to previous theoretical and experimental investigations on neutral PAH molecules and provides new guidelines for identifying which superhydrogenated states of a curved aromatic molecule, such as corannulene, are expected to be present in interstellar environments. The inclusion of these superhydrogenated species in astrochemical models may give rise to a more realistic picture of the interstellar chemistry involving PAHs. Furthermore, the investigation of curved PAHs may also provide a better understanding of some spectral features of the ISM. For example, non-planar components of PAHs such as corannulene have been suggested to be the origin of some spectral features of the AIBs. Last but not least, this work also has important consequences for the top–down formation of fullerenes as H-atom interaction of the intermediates (such as corannulene-like species) is inevitable and hence needs to be considered in astrochemical models.

ACKNOWLEDGEMENTS

This work has been supported by the E.U. under the Horizon 2020 Marie Sklodowska-Curie ITN EUROPAH (grant agreement no. 722346) and the Danish National Research Foundation through the Center of Excellence 'InterCat' (grant agreement no. DNRF150). We also acknowledge financial support from the Danish Council for Independent Research (grant no. 5137-00049B), the European Research Council (CoG GRANN, grant agreement no. 648551). We thank the CINECA award NEQRate under the ISCRA initiative for the availability of high performance computing resources and support.

DATA AVAILABILITY

The data underlying this article are available at the following repository https://datadryad.org/stash/share/AxcZfHMxW-650pD4FJCd-oEp24hvF0Im8z_jwiltrzs.

REFERENCES

Bakes E. L. O., Tielens A. G. G. M., 1998a, ApJ, 499, 258
Bakes E., Tielens A., 1998b, ApJ, 499, 258
Bauschlicher C. W., Jr, 1998, ApJ, 509, L125
Becker L., Bunch T., 1997, Meteorit. Planet. Sci., 32, 479
Bernal J., Haenecour P., Howe J., Zega T. J., Amari S., Ziurys L. M., 2019, ApJ, 883, L43
Berné O., Tielens A. G., 2012, Proc. Natl. Acad. Sci., 109, 401
Bernstein L., Shroll R. M., Galazutdinov G. A., Beletsky Y., 2018, ApJ, 859, 174
Bonfanti M., Casolo S., Ponti A., Tantardini G., Martinazzo R., 2011, J. Chem. Phys., 135, 164701
Bouwman J., de Haas A. J., Oomens J., 2016, Chem. Commun., 52, 2636
Cami J., Bernard-Salas J., Peeters E., Malek S. E., 2010a, Science, 329, 1180
Cami J., Bernard-Salas J., Peeters E., Malek S. E., 2010b, Science, 329, 1180
Cami J., Peeters E., Bernard-Salas J., Doppmann G., De Buizer J., 2018, Galaxies, 6, 101
Campbell E. K., Holz M., Gerlich D., Maier J. P., 2015, Nature, 523, 322
Campisi D., Simonsen F. D. S., Thrower J. D., Jaganathan R., Hornekær L., Martinazzo R., Tielens A. G. G. M., 2020, Phys. Chem. Chem. Phys., 22, 1557
Candian A., Zhen J., Tielens A. G. G. M., 2018, Phys. Today, 71, 38
Casolo S., Martinazzo R., Bonfanti M., Tantardini G., 2009, J. Chem. Phys. A, 113, 14545
Cassam-Chenaï P., Pauzat F., Ellinger Y., 1994, AIP Conference Proceedings. AIP, New York, p. 543
Cazaux S. et al., 2016, Sci. Rep., 6, 19835

Cazaux S., Arribard Y., Egorov D., Palotás J., Hoekstra R., Berden G., Oomens J., Schlathölter T., 2019, ApJ, 875, 27
Clar E., 1972, The Aromatic Sextet. Wiley, New York
Crowley C., Kroto H. W., Taylor R., Walton D. R., Bratcher M. S., Cheng P.-C., Scott L. T., 1995, Tetrahedron Letters, 36, 9215
De Haas A. J., Oomens J., Bouwman J., 2017, Phys. Chem. Chem. Phys., 19, 2974
Duley W. W., 2006, Faraday Discussions, 133, 415
Evans M. G., Polanyi M., 1938, Trans. Faraday Soc., 34, 11
Fan G., Manson J., 2009, Phys. Rev. B, 79, 045424
Ferullo R. M., Zubieta C. E., Belelli P. G., 2019, Phys. Chem. Chem. Phys., 21, 12012
Frisch M. J. et al., 2016, Gaussian∼ 16 Revision C.01. Gaussian Inc. Wallingford CT
Gaboardi M., Pratt F., Milanese C., Taylor J., Siegel J., Fernandez-Alonso F., 2019, Carbon, 155, 432
Galuè A. H., Leines D. G., 2017, Phys. Rev. Lett., 119, 171102
Galué H. A., Rice C. A., Steill J. D., Oomens J., 2011, J. Chem. Phys., 134, 054310
Gatchell M. et al., 2015, Phys. Rev. A, 92, 050702
Grimmelmann E. K., Tully J. C., Cardillo M. J., 1980, J. Chem. Phys., 72, 1039
Hornekaer L. et al., 2006, Phys. Rev. Lett., 96, 156104
Ioppolo S., Fedoseev G., Lamberts T., Romanzin C., Linnartz H., 2013, Rev. Sci. Ins., 84, 073112
Jaganathan R., Simonsen F. D. S., Thrower J. D., Hornekær L., 2022, A&A, 663, A136
Jensen P. A., Leccese M., Simonsen F. D. S., Skov A. W., Bonfanti M., Thrower J. D., Martinazzo R., Hornekær L., 2019, MNRAS, 486, 5492
Jochims H., Baumgärtel H., Leach S., 1999, ApJ, 512, 500
Karadov P. B., 2016, Chem. Phys. Lett., 646, 190
Kroto H., 1988, Science, 242, 1139
Léger A., d'Hendecourt L., 1985, A&A, 146, 81
Leger A., Puget J., 1984, A&A, 500, 279
Le Page V., Snow T. P., Bierbaum V. M., 2003, ApJ, 584, 316
Lovas F. J., McMahon R. J., Grabow J.-U., Schnell M., Mack J., Scott L. T., Kuczkowski R. L., 2005, J. Am. Chem. Soc., 127, 4345
Mennella V., HornekæR L., Thrower J., Accolla M., 2011, ApJ, 745, L2
Mennella V., Suhasaria T., Hornekær L., Thrower J., Mulas G., 2021, ApJ, 908, L18
Nestoros E., Stuparu M. C., 2018, Chem. Commun., 54, 6503
Omont A., Bettinger H. F., 2021, A&A, 650, 13
Peeters E., Mattioda A. L., Hudgins A. L., Allamandola L. J., 2004, A&A, 617, 65
Petrignani A., Vala M., Eyler J., Tielens A., Berden G., Van der Meer A., Redlich B., Oomens J., 2016, ApJ, 826, 33
Pilleri P. et al., 2009, MNRAS, 397, 1053
Pope C. J., Marr J. A., Howard J. B., 1993, J. Phys. Chem., 97, 11001
Rapacioli M., Cazaux S., Foley N., Simon A., Hoekstra R., Schlathölter T., 2018, Phys. Chem. Chem. Phys., 20, 22427
Rauls E., Hornekær L., 2008, ApJ, 679, 531
Reitsma G., Boschman L., Deuzeman M., González-Magaña O., Hoekstra S., Cazaux S., Hoekstra R., Schlathölter T., 2014, Phys. Rev. Lett., 113, 053002
Salama F., 2008, Proc. Int. Astron. Un., 4, 357
Scanlon L. et al., 2006, J. Phys. Chem. B, 110, 7688
Simonsen F. D. S., 2020, PhD thesis, Aarhus University
Skov A. L., Thrower J. D., Hornekaer L., 2014, Faraday Discussions, 168, 223
Stockett M. H. et al., 2021, ApJ, 913, 46
Sundararajan P., Tsuge M., Baba M., Lee Y.-P., 2018, ACS Earth Space Chem., 2, 1001
Tang Z., Simonsen F. D. S., Jaganathan R., Palotás J., Oomens J., Hornekær L., Hammer B., 2022, A&A, 663, A150
Thaddeus P., 2006, Phil. Trans. Roy. Soc. B: Biol. Sci., 361, 1681
Thrower J. D. et al., 2012, ApJ, 752, 3
Thrower J. D., Friis E. E., Skov A. L., Jørgensena B., Hornekaer L., 2014, Phys. Chem. Chem. Phys., 16, 3381
Tielens A. G. G. M., 2008, A&A, 46, 289
Tielens A. G. G. M., 2013, Rev. Modern Phys., 85, 1021
Tschersich K., Fleischhauer J., Schuler H., 2008, J. Appl. Phys., 104, 034908
West B., Useli-Bacchitta F., Sabbah H., Blanchet V., Bodi A., Mayer P. M., Joblin C., 2014, J. Phys. Chem. A, 118, 7824
Wolf M., Kiefer H., Langeland J., Andersen L., Zettergren H., Schmidt H. T., Cederquist H., Stockett M., 2016, ApJ, 832, 24
Zhao Y., Thrular D. G., 2008, Theor. Chem. Accounts, 120, 215
Zhao L. et al., 2019, Phys. Chem. Chem. Phys., 21, 16737
Zhao L. et al., 2021, Phys. Chem. Chem. Phys., 23, 5740

APPENDIX A: CLAR'S STRUCTURES

A Clar's formula is a Kekulè resonance structure with the maximal number of aromatic π-sextet (C), that is, benzene-like moieties. Clar's rule states that Clar's formula are the most important among resonance structures in determining the properties of PAHs (Clar 1972).

For pristine corannulene, $C = 2$, and one can realize up to five Clar's formulae ($r_C = 5$) as shown in Fig. A1. As H-atoms are attached to the molecule, the number of realizable resonance structures involving two Clar's sextets progressively reduce. In particular, for $n = 4$, one can draw just two Clar's formulae with $C = 2$. Hence, $r_C = 2$ for $n = 4$. Looking at the hydrogenation sequence for corannulene in Figs 3 and 4, we note that up to the 8th step, the reaction proceeds in such a way that the maximum number of Clar's sextet ($C = 2$) is preserved. The sticking of the 9th H-atom, regardless of the position, results in the reduction of such a number from 2 to 1 while sticking of the 15th H-atom results in further reduction to 0.

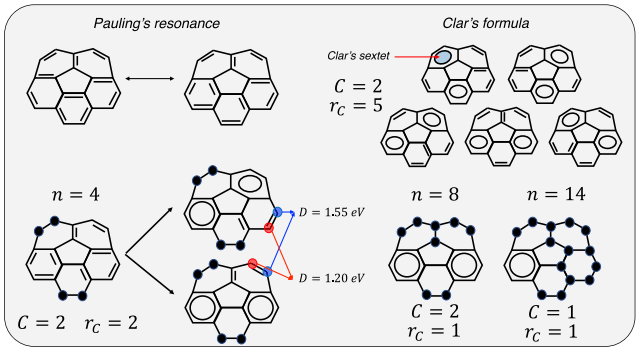

Figure A1. Pictorial representation of Clar's structures for corannulene and superhydrogenated corannulene with $n = 4$, 8, and 14. C is the maximal Clar's number, r_C is the number of resonance structures with the maximal Clar's number that one can draw.

APPENDIX B: PYRAMIDALIZATION

Consider a three-coordinated C atom and let $\hat{n}_i$ ($i = 1, 2, 3$) be the unit vectors directed towards its closest neighbours. Then

$$\hat{n}_1 \cdot \hat{n}_2 = \cos(\theta_{12}) \tag{B1}$$

defines the bond angle θ_{12} between the σ-bond 1 and 2 (assuming that they are not bent) and similarly for θ_{23}, θ_{13}. For an ideal sp^2 carbon atom, $\theta_{ij} = 120°$, the bonds lie on a plane and the normal of the plane defines the direction of the π orbital – the 'π axis' – that forms equal angles with the $\hat{n}_i$'s (Fig. B1). For general curved structures, one can yet define a similar axis, based solely on geometric considerations: if the $\hat{n}_i$'s are not co-linear there exists a unique axis $\hat{q}$ that form equal angles with the $\hat{n}_i$'s, i.e. such that $\hat{q}\hat{n}_i = \cos(\alpha)$ holds for $i = 1-3$.

Upon choosing the direction of that axis in such a way that $\alpha \geq \pi/2$, the pyramidalization angle is defined as $\theta_P = \theta_\alpha - \pi/2$. For sp^2 carbon atoms $\theta_P \equiv 0$, while for an sp^3 carbon atom, $\theta_P \approx 19.5^\circ$, since the π-axis points evidently along an sp^3 orbital and the σ-bonds make an angle of 109.5° with each other. A pyramidalization angle in the range $0 < \theta_P < 19.5^\circ$ thus indicates a mixed sp^2–sp^3 orbital configuration. The latter manifests itself through a change in the balance between the σ (sp^2) and π (p) hybridization. In particular, π-orbitals acquire a fractional s-component while sp^2 orbitals deviate from such a purely integer hybridization. The extent of such rehybridization can be determined by resorting to the so-called Coulson's directionality theorem that defines a π-axis generally *different* from the geometric one introduced above. This axis is the direction where the π-like orbital at the C atom points to, hence defines the 'local geometry' of the π-cloud in a (possibly curved) π-system.

Consider a carbon atom using some kind of sp^τ hybrids to form σ bonds with its three neighbours. The (unnormalized) hybrids can be represented in the form

$$|\psi_i\rangle = |s\rangle + \sqrt{\tau_i}|p_i\rangle, \tag{B2}$$

where $|s\rangle$ describes a s orbital and $|p_i\rangle$ a *directional* p orbital pointing along the bond, while τ_i is the fraction of p character in the hybrid, also called hybridization index. Since hybrids are orthogonal to each other

$$\langle\psi_i|\psi_j\rangle = 1 + \sqrt{\tau_i \tau_j}\cos(\theta_{ij}) \propto \delta_{ij}, \tag{B3}$$

where θ_{ij} is the corresponding bond angle. Therefore, the hybridization indices can be computed from the bond angles as

$$\cos(\theta_{ij}) = -\frac{1}{\sqrt{\tau_i \tau_j}} \quad i \neq j. \tag{B4}$$

With three σ bonds and three hybrids involved in their formation, there remains a fourth orbital that is orthogonal to all them. This is the hybrid left for π bonding, and its hybridization index λ can then be obtained from the conservation of p (or s) weights upon hybridization, e.g.

$$\lambda = \frac{1}{1 - \sum_{i=1}^{3}(1+\tau_i)^{-1}} - 1. \tag{B5}$$

(This expression is singular, as it should be, for co-planar σ-bonds.) Knowledge of λ allows one to determine the angles that the π-like orbital forms with the σ-bonds; hence, the orientation of the (true) π-axis in space.

When comparing sites with same π-coordination and comparable pyramidalization ($\Delta\theta_P < 2 - 3^\circ$), as happens for outer-edge and inner-edge,[2] the H-addition occurs preferentially on outer-edge sites. This is well illustrated, for instance, by the fifth or ninth step (see Fig. B2). At the fifth hydrogenation, the most pyramidalized sites are the central carbon atoms[3] which have π-coordination $Z = 3$. Among inner-edge sites, there are four sites with $Z = 2$, those close to the previously hydrogenated positions. Because of the smaller π-coordination, these sites display greater binding energies (D = 1.43 eV) than inner-edge with $Z = 3$ (D = 0.63 eV). However, the pyramidalization of these sites is still limited (≈4.2°), and the reaction occurs on an outer-edge site (as for the first H-addition). Also noteworthy is that the H-atom attaches to the most pyramidalized site among the outer-edge sites. On the other hand, at the ninth step, sites on the inner 5-membered ring with $Z = 2$ and $\theta_P > 6$ are available and the H-atom sticks indeed on the carbon atom with the largest pyramidalization angle. Overall, the H-attachment on specific lattice positions is determined by a delicate interplay between coordination and pyramidalization.

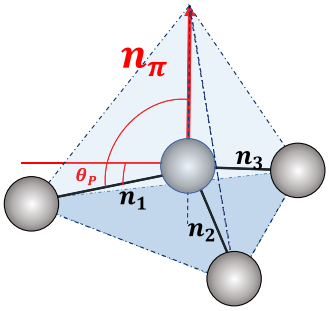

Figure B1. Pictorial representation of the pyramidalization angle θ_P. $\hat{n}_\pi$ is the π-orbital axis vector, while $\hat{n}_i$ ($i = 1, 2, 3$) are unit vectors directed along the three σ-bond.

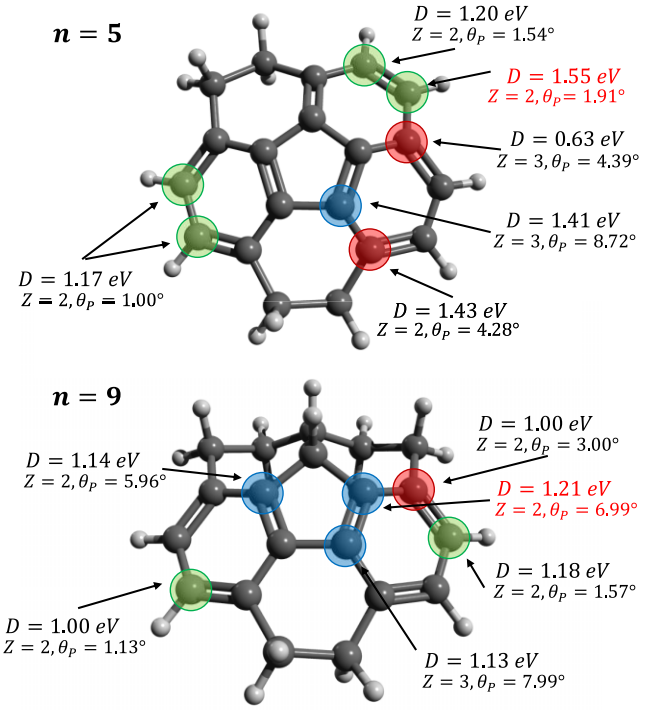

Figure B2. Binding energies for some sites that were checked at the fifth ($n = 5$) and ninth ($n = 9$) hydrogenation levels. For each site, the π-coordination (Z) and the pyramidalization angle (θ_P) are reported. Green, red, and blue circle mark outer edge, inner edge, and centre sites, respectively.

APPENDIX C: OPTIMIZED STRUCTURES OF *n*H-CORANNULENE

We have found two feasible sequences for adding a H-atom to every carbon atom in corannulene. A first sequence wherein the first H-

[2]Here, an outer-edge site is intended as a site on the edge that binds two carbon atoms. Therefore, during the hydrogenation, an outer-edge site remains so, regardless of the presence of hydrogenated nearest-neighbours. The same applies to inner-edge sites.

[3]Note that, as for the first H-addition, these sites are still characterized by relatively large binding energies, when compared to the outer-edge sites.

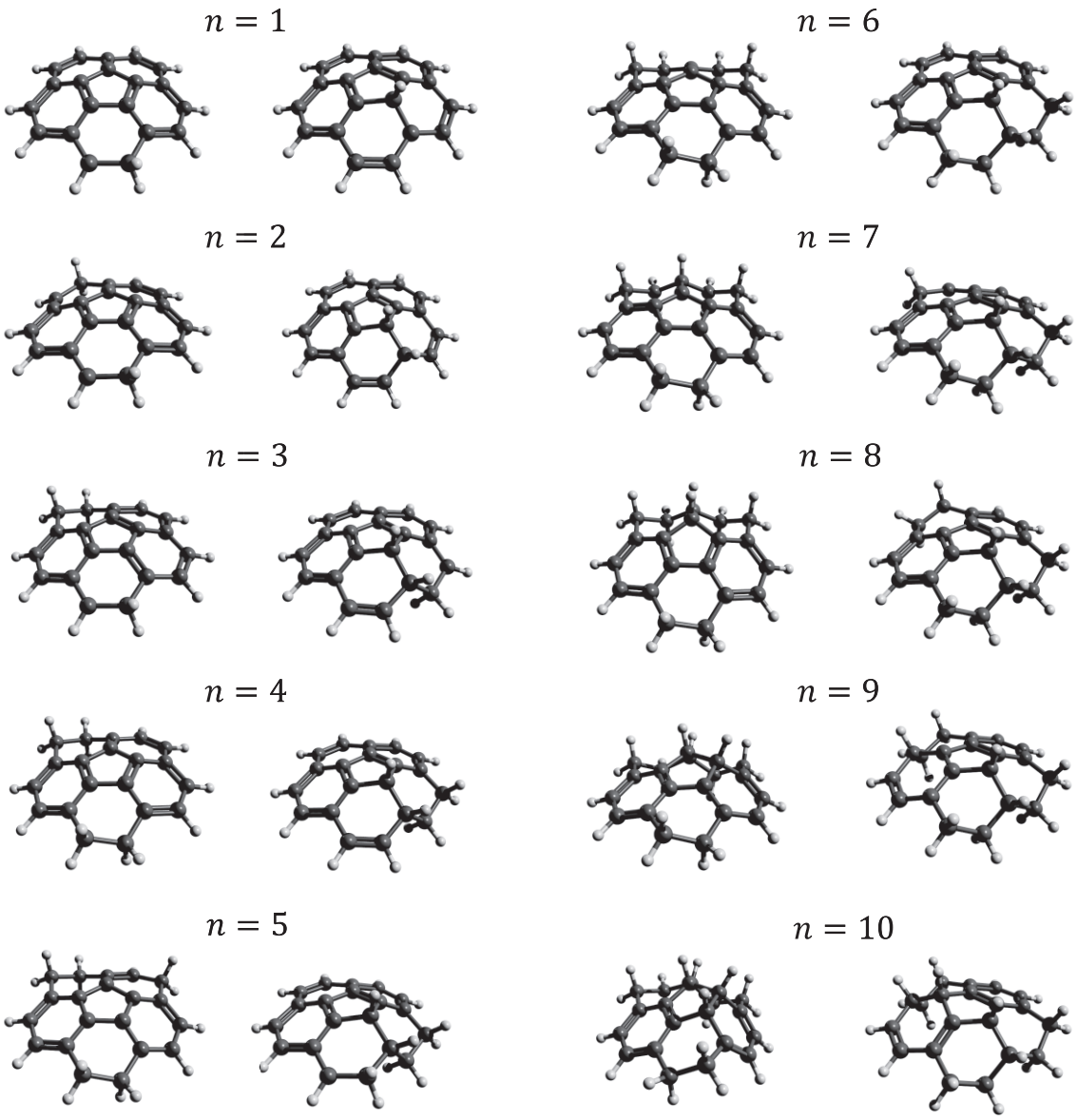

Figure C1. Optimized structures for $n = 1$ to $n = 10$ of the first (left) and the second (right) hydrogenation sequence discussed in the main text.

atom attaches to the outer-edge and a second sequence wherein the first H-atom attaches to the centre site. Even though from the $n = 15$ onwards the hydrogenation sites are the same on the C-lattice, the energetics along the two pathways display some differences. The reason is that, along the two hydrogenation pathways, the corannulene molecule distorts in different ways, as it is shown in Figs C1 and C2. Therefore, even if, e.g. the 19th site of hydrogenation is the same in both sequences, its local neighbourhood differs in terms of Gaussian curvature, carbon atom hybridization among other things (see Fig. C3). This, in turn, leads to different binding energies and sticking barriers.

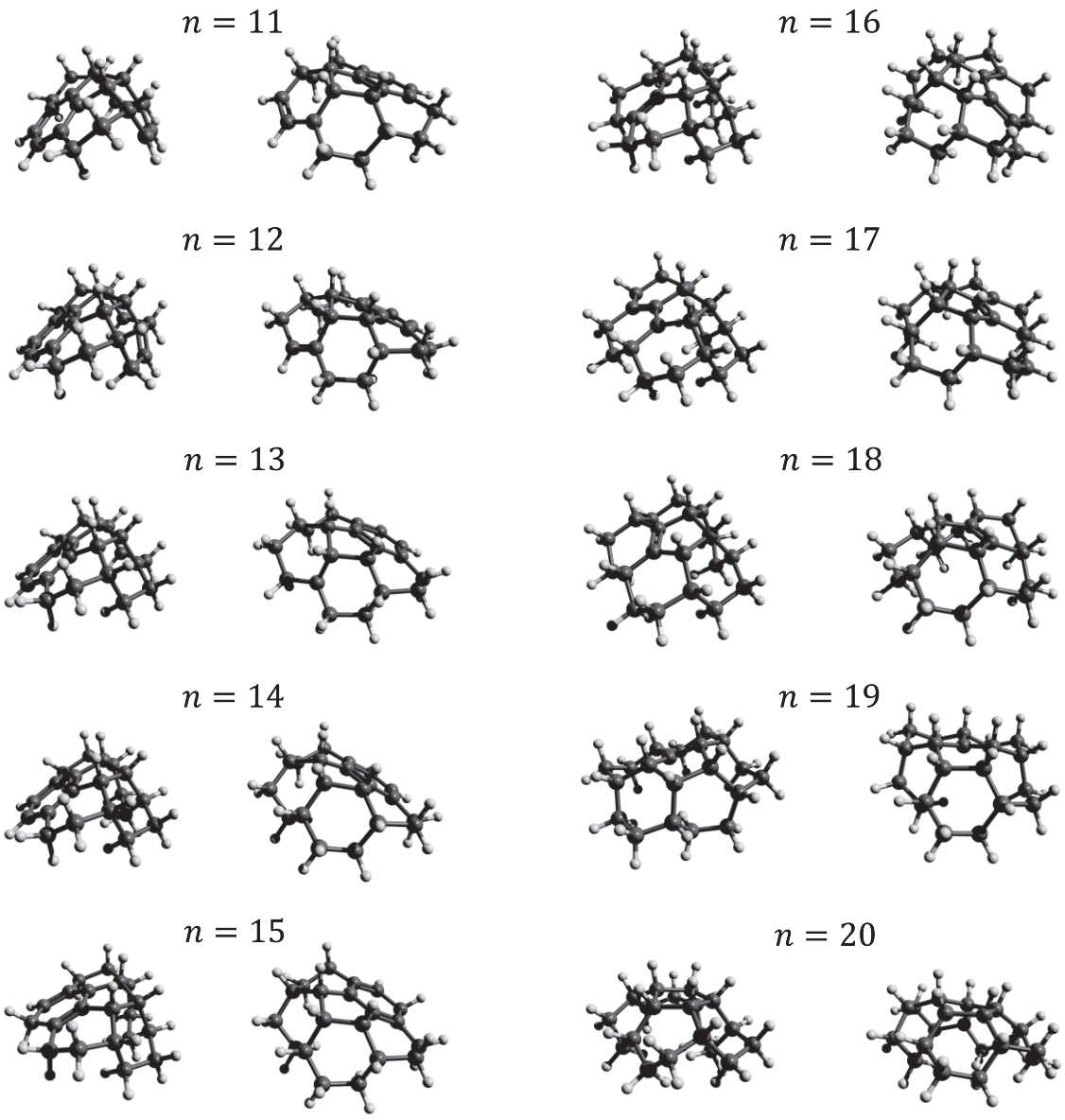

Figure C2. Optimized structures for $n = 11$ to $n = 20$ of the first (left) and the second (right) hydrogenation sequence discussed in the main text.

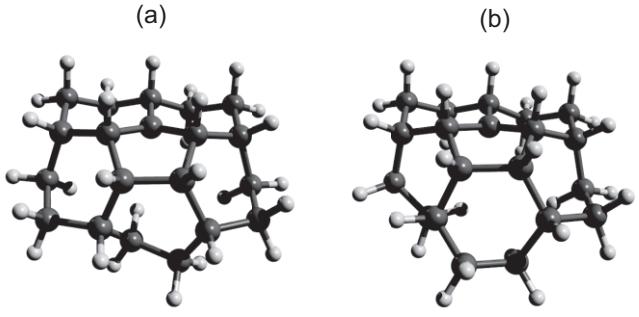

Figure C3. Structure with $n = 19$ in the first path (a) and in the second path (b).

This paper has been typeset from a TEX/LATEX file prepared by the author.